

# Comparative Electron and Photon Excitation of Localized Surface Plasmon Resonance in Lithographic Gold Arrays for Enhanced Raman Scattering

*Yitian Zeng<sup>† \*</sup>, Steven J. Madsen<sup>†</sup>, Andrew B. Yankovich<sup>‡ \*</sup>, Eva Olsson<sup>‡</sup>, and Robert Sinclair<sup>† \*</sup>*

<sup>†</sup>Department of Materials Science and Engineering, Stanford University, Stanford, California  
94305, United States.

<sup>‡</sup>Department of Physics, Chalmers University of Technology, Gothenburg 41296, Sweden.

Supplementary Information

## 1. Points of Interest Analysis on Nanoparticle Size and LSPR

STEM-EELS is a scanning based technique, which is inherently slow due to the serial nature of the image acquisition. Mapping an area shown in **main text Fig. 1** insets generally takes at least 40 minutes with our S/TEM. In order to survey a large number of different particle sizes, points of interest analysis were introduced based on the features of the collected EELS maps to reduce the experimental time. **Fig. S1** shows the ADF-STEM images of nanodisc arrays with a constant edge to edge separation of 90 nm and disc diameters ranging from 50 nm to 200 nm. Four 8 nm by 8 nm square regions (**Fig. S1** schematic) located around the north, south, east and west perimeter of the disc were examined under the electron probe and a total of 64 EEL spectra were averaged to derive the localized surface plasmon energy. Similarly, a line scan of triangle sides was recorded for each bowtie pattern with triangle height varied from 70 nm to 220 nm in **Fig. S2**. EEL spectra near the tip and middle point regions were analyzed separately. The measured dipolar LSPR peak energies of each pattern on silicon nitride and silicon oxide membranes are plotted as a function of nanoparticle size in **main text Fig. 3c and 6b**.

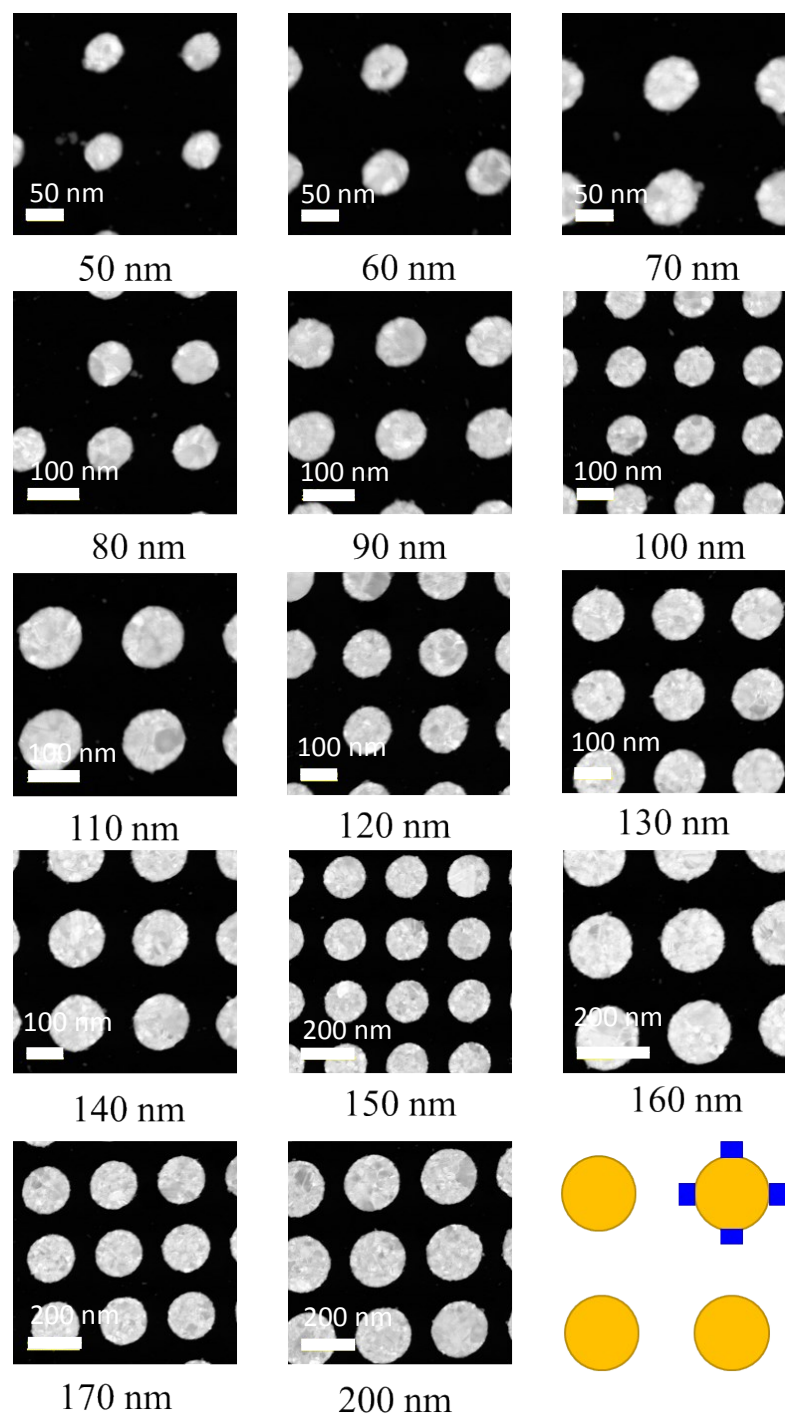


**Fig. S1** ADF-STEM images of gold nanodisc arrays with the same edge to edge spacing of 90 nm and diameters from 50 nm to 200 nm. Blue boxed regions (8 nm by 8 nm) in the schematic indicate where the EEL spectra were collected.

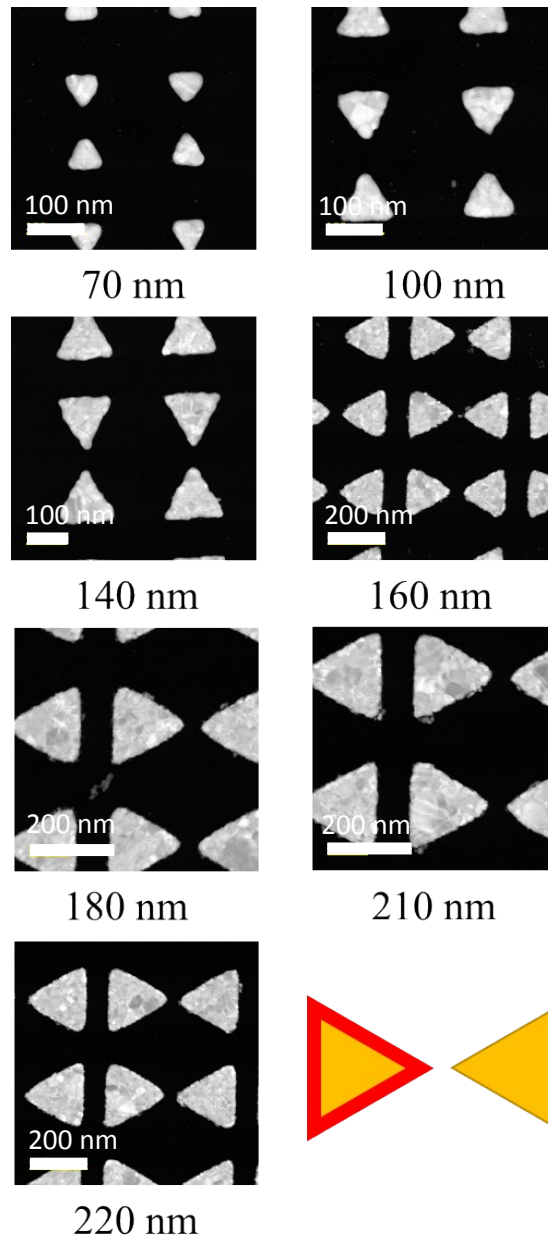


**Fig. S2** ADF-STEM images of bowtie arrays with the same point to point interspacing of 20 nm and triangle height (size) from 70 nm to 220 nm. The line scan (2 nm in width) along triangle sides is indicated in the schematic.

## 2. Effect of Surrounding Dielectric Environment on LSPR

From classical electromagnetic theory using the simple quasi-static approximation provided that  $d \ll \lambda$  (i.e. the particle is much smaller than the wavelength of light in the surrounding medium), we can study the interaction of a metallic nanoparticle with the electromagnetic field by solving the Laplace equation for the potential,  $\nabla^2 \phi = 0$ <sup>1</sup>. The general solution for a spherical nanoparticle<sup>2</sup> implies that the applied field induces

a dipole moment inside the nanoparticle with the polarizability  $\alpha = 4\pi a^3 \frac{\epsilon - \epsilon_m}{\epsilon + 2\epsilon_m}$ .  $a$  is the nanoparticle

radius,  $\epsilon$  is the dielectric function of the metallic nanoparticle which is strongly dependent on the incident frequency (in the visible range for gold and silver).  $\epsilon_m$  is the dielectric constant of the surrounding media.

It is apparent that the polarizability experiences a resonant enhancement when the denominator  $\epsilon(\omega_p) + 2\epsilon_m = 0$ , known as the Fröhlich condition<sup>3</sup>. The associated mode in an oscillating electric field is called the dipolar surface plasmon of the metal nanoparticle, where  $\omega_p$  is the theoretical LSPR frequency.

Therefore, the LSPR is strongly affected by the surrounding medium as the dielectric constant differs for  $\text{SiN}_x$  ( $\sim 4.2$ ) and  $\text{SiO}_x$  ( $\sim 2.1$ ) in the visible wavelength regime. **Fig. S3a** shows the dielectric function

$\epsilon(\omega)$  of Au (black curve) and  $-2\epsilon_m$  constants of  $\text{Si}_3\text{N}_4$  (red line) and  $\text{SiO}_2$  (blue line). The two intersections ( $\epsilon(\omega) = -2\epsilon_m$ ) correspond to their respective Fröhlich condition and illustrate that the LSPR red-shifts as

the surrounding dielectric constant  $\epsilon_m$  is increased. We re-plotted **main text Fig. 3c** in reverse axes in **Fig.**

**S3b** for comparison between the theoretical surface plasmon frequency and the measured values. As **Fig.**

**S3a and b** share the same scale along the horizontal axes, we found that the LSPR from smaller nanodisc arrays are closer to the theoretical values as indicated by dotted vertical lines, which is consistent with the quasi-static assumption.

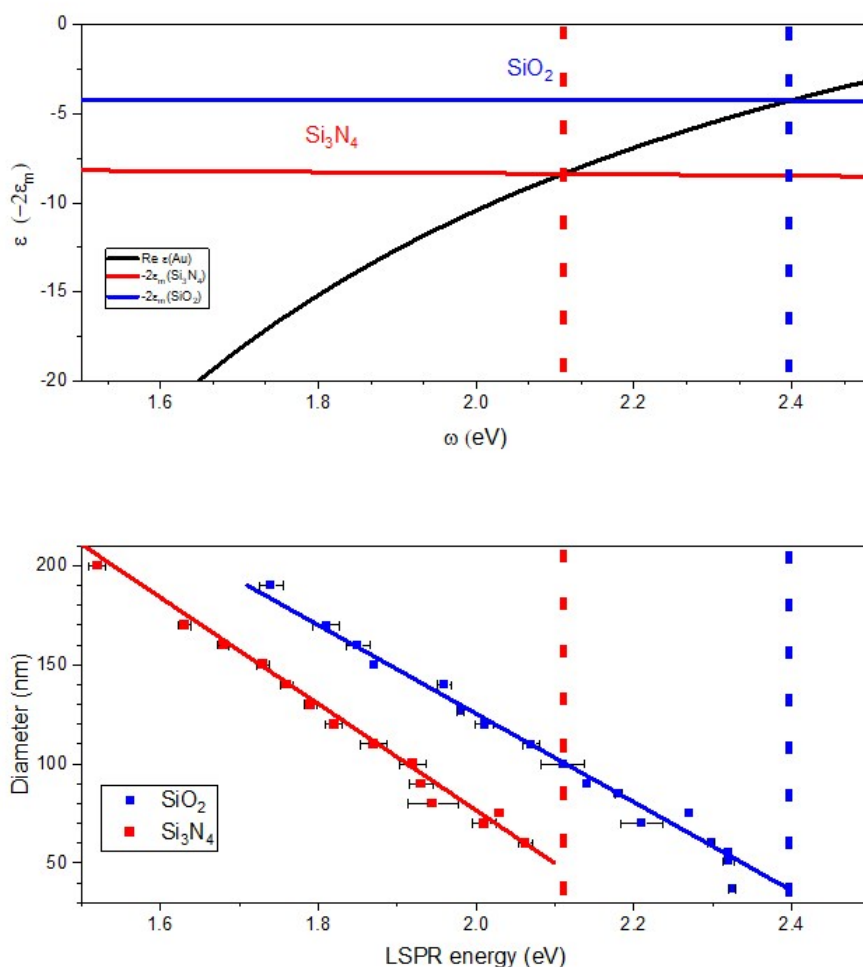


**Fig. S3** (a) Dielectric function  $\epsilon(\omega)$  of Au (black curve) and  $-2\epsilon_m$  constants of  $\text{Si}_3\text{N}_4$  (red line) and  $\text{SiO}_2$  (blue line). The frequency of the two intersections represents the theoretical LSPR for Au nanoparticles on  $\text{Si}_3\text{N}_4$  and  $\text{SiO}_2$ . (b) Measured dipolar LSPR blue shifts as nanodisc diameter is decreased for  $\text{Si}_3\text{N}_4$  and  $\text{SiO}_2$  (replotted from **main text Fig. 3c** in reverse axes). (a) and (b) share the same scale along the horizontal axis. Together it shows that LSPR from smaller arrays are closer to the theoretical values as indicated by dotted vertical lines.

### 3. Additional Rhodamine 6G (R6G) Raman Spectra on Nanodisc Arrays

**Fig. S4** shows Raman spectra of 10 mg/mL R6G (molecular weight: 479 g/mol) water solution in a cuvette with 1 mm optical path as a control sample collected using a 638 nm laser. The laser spot size is estimated to be 2  $\mu\text{m}$  in diameter, the liquid thickness is 1 mm, therefore approximately  $4 \times 10^{10}$  R6G molecules contributed to the control Raman spectra. This is later used to calculate Raman enhancement factors.

**Fig. S5** shows Raman spectra of R6G attached to 75 nm diameter nanodiscs on a silicon nitride substrate with different interspacing illuminated by a 638 nm laser. Overall, smaller interspacing arrays exhibit slightly stronger Raman peaks with the strongest being for the nanodiscs separated by 35 nm owing to stronger near field interaction and closer matching to the illuminating laser energy. Additionally, the overall number of nanoparticles in the same area is also larger for smaller interspacing arrays, which contributes to a larger Raman cross-section.

**Fig. S6** shows R6G Raman spectra of different size nanodisc arrays on a silicon nitride membrane under far off-resonance excitation situations. When using a 785 nm laser, the illumination energy is lower than the LSPR peak energy of all nanodiscs investigated. Therefore, Raman spectra are mostly dominated by noise with two signature Raman peaks at 1181 and 1361  $\text{cm}^{-1}$  barely distinguishable in 90 nm and 150 nm arrays, shown in **Fig. S6a**. When using a 532 nm laser in **Fig. S6b**, the SERS signal is stronger from smaller diameter arrays similarly due to a smaller difference between the laser energy and LSPR.

**Fig. S7** shows R6G Raman spectra of different size nanodisc arrays on a silicon oxide membrane measured with a 638 nm laser. In the **main text Fig. 3b**, the LSPR of 150 nm nanodiscs lies in the Raman collection region of the 638 nm laser, while the rest have higher energy than the laser excitation energy. The measured

Raman spectra follow the same behavior as shown in the **main text Fig. 5**, with strongest Raman signal enhancement coming from the 150 nm diameter nanodisc array.

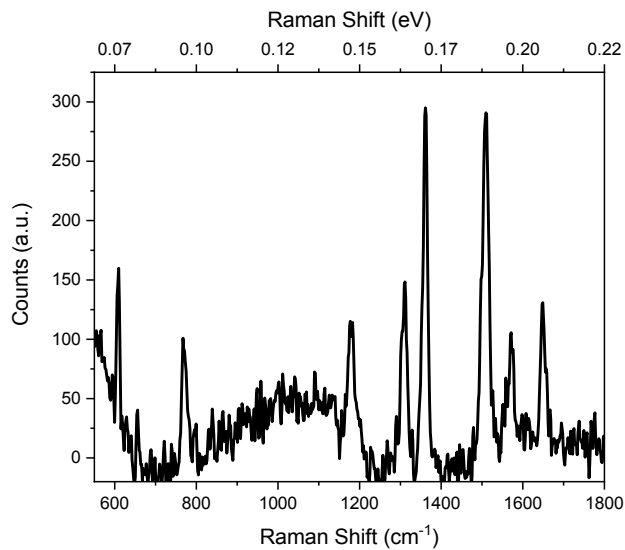


**Fig. S4** Raman spectra of 10 mg/mL R6G water solution in a cuvette with 1 mm optical path as a control sample collected using a 638 nm laser. Approximately  $4 \times 10^{10}$  R6G molecules are probed under these situations.

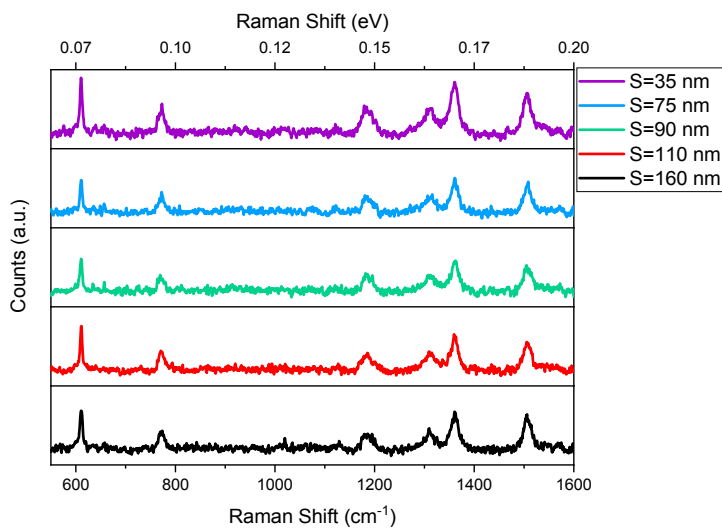


**Fig. S5** R6G Raman spectra of 75 nm nanodisc arrays on silicon nitride substrates with different interspacing illuminated by a 638 nm laser showing that smaller interspacing arrays exhibit slightly stronger Raman peaks with the strongest being nanodiscs separated 35 nm apart.

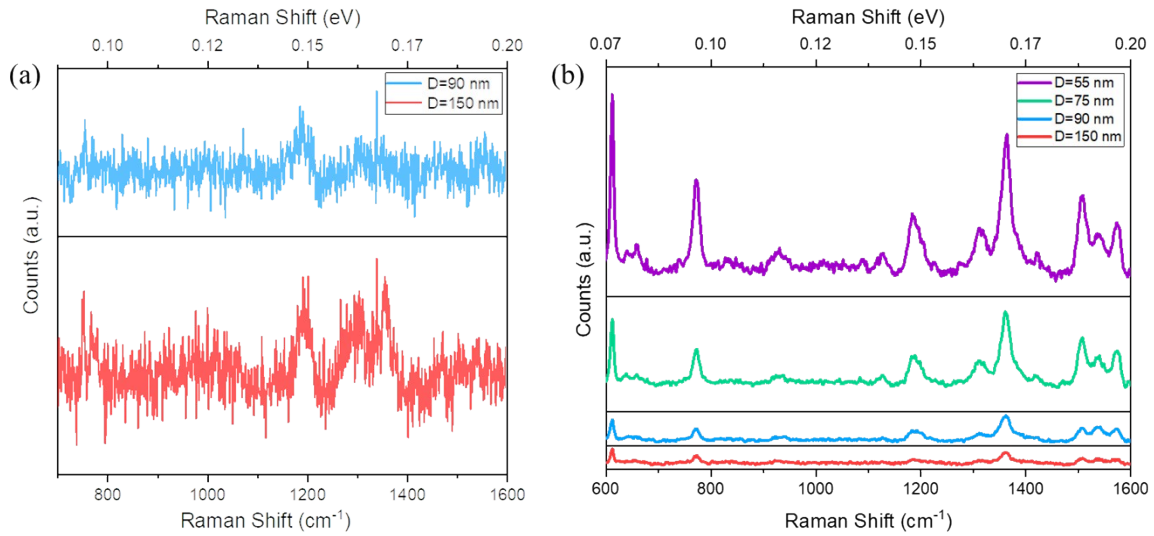


**Fig. S6** R6G Raman spectra of different size nanodiscs (90 nm edge to edge separation) on  $\text{SiN}_x$  substrates measured (a) with a 785 nm laser ( $\sim 8$  mW) showing mostly noise due to inefficient surface plasmon excitation and (b) with a 532 nm laser ( $\sim 0.6$  mW) showing that the Raman enhancement is stronger for smaller diameter arrays due to a smaller difference between the laser energy and LSPR. The total acquisition time is 2 mins.

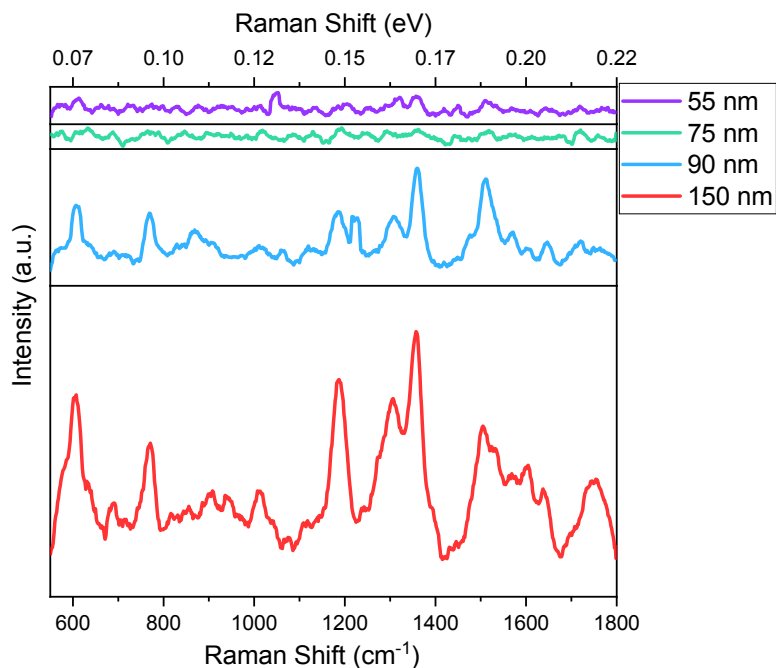


**Fig. S7** R6G Raman spectra of different diameter nanodiscs on a SiO<sub>x</sub> membrane measured with a 638 nm laser. The strongest Raman enhancement comes from the 150 nm diameter nanodiscs because the LSPR is close to the laser energy and within the Raman collection band.

#### 4. 4-Mercaptopyridine (4-MP) Raman Spectra on Nanodisc Arrays

We also used 4-MP as the probe molecule to characterize the Raman signal enhancement in addition to R6G. The thiol group of 4-MP is believed to be chemisorbed onto the Au surface and creates a more even coverage. The observed trend on the same series of nanodisc arrays follows closely to those with R6G, suggesting that the enhancement provided by the nanoparticles is independent of the type of Raman dye.

**Fig. S8** shows Raman spectra of 4-MP attached to different size nanodisc arrays on a silicon nitride membrane measured with different laser wavelengths. The trend of observed Raman signal enhancement is similar to that of R6G on the same size series of nanodisc arrays (main text **Fig. 5**), although the overall Raman signal counts are lower than for R6G due to the comparatively smaller Raman cross section of the

4-MP molecule. When using a 638 nm laser (**Fig. S8a**), the illumination energy is close to the LSPR of 90 nm diameter nanodiscs, resulting in strongest Raman signal enhancement. When using a 532 nm laser in **Fig. S8b**, the SERS signal is stronger from smaller diameter arrays similarly due to a smaller difference between the laser energy and their LSPR.

**Fig. S9** shows the 4-MP Raman spectra of nanodisc arrays with different interspacing on a SiN<sub>x</sub> membrane measured with different laser wavelengths. Similar to R6G Raman spectra on the same series of arrays (main text **Fig. 4** and **Fig. S5**), they show similar Raman signal intensity overall, with slightly stronger Raman enhancement for arrays with smaller interspacing.

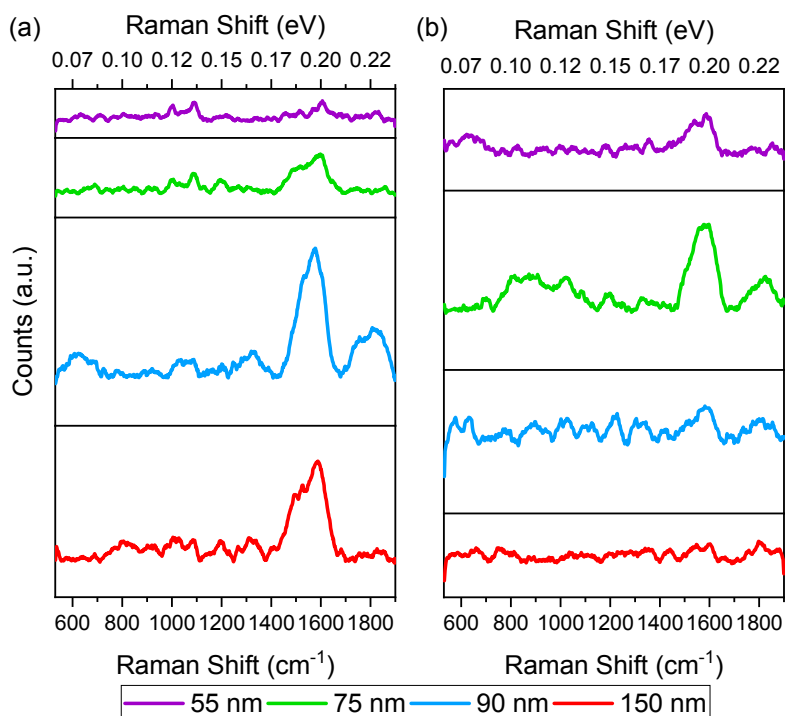


**Fig. S8** 4-MP Raman spectra of different sized nanodisc arrays on a SiN<sub>x</sub> membrane measured with **(a)** a 638 nm laser and **(b)** a 532 nm laser. Nanodiscs with 90 nm diameter shows strongest Raman signals when illuminated with a 638 nm laser, while smaller sized arrays show stronger signals when illuminated with a 532 nm laser because their LSPR is close to the laser excitation energy.

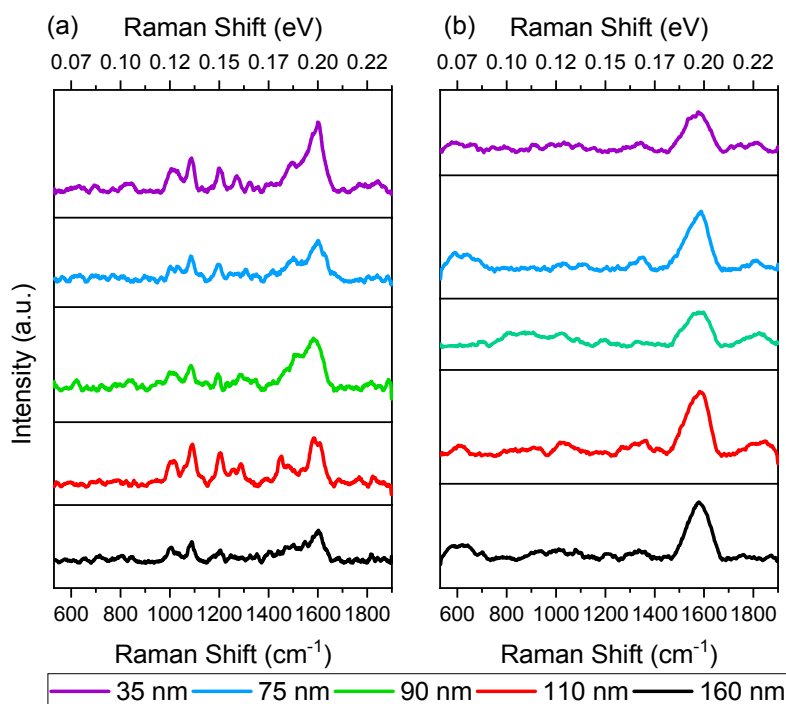


**Fig. S9** 4-MP Raman spectra of nanodisc arrays with different interspacing on a SiN<sub>x</sub> membrane measured with **(a)** a 638 nm laser and **(b)** a 532 nm laser. These arrays show similar Raman signal intensity overall, with slightly stronger Raman enhancement for arrays with smaller interspacing.

## 5. Laser Power

A Horiba XploRa+ confocal Raman microscope is equipped with a 532 nm laser (60 mW), a 638 nm laser (17 mW) and a 785 nm laser (80 mW). A neutral density filter (NDF) is used to adjust the output power to optimize the spectra collection procedure. Exposing a pristine pattern of nanodisc arrays (**Fig. S10a**) to a focused 532 nm laser (50% NDF, 30 mW) for 4 minutes would cause irreversible deterioration (**Fig. S10b, c**) due to local heating, hence a strong decrease of Raman signal enhancement. Exposure to a much lower laser intensity would increase the noise level and make the acquisition undesirably long. Therefore, we optimized the laser power with 1%, 10% and 10% NDF to output 0.6 mW, 1.7 mW and 8 mW for the 532 nm laser, 638 nm laser and 785 nm laser respectively, and avoided the damage shown in **Fig. S10**.

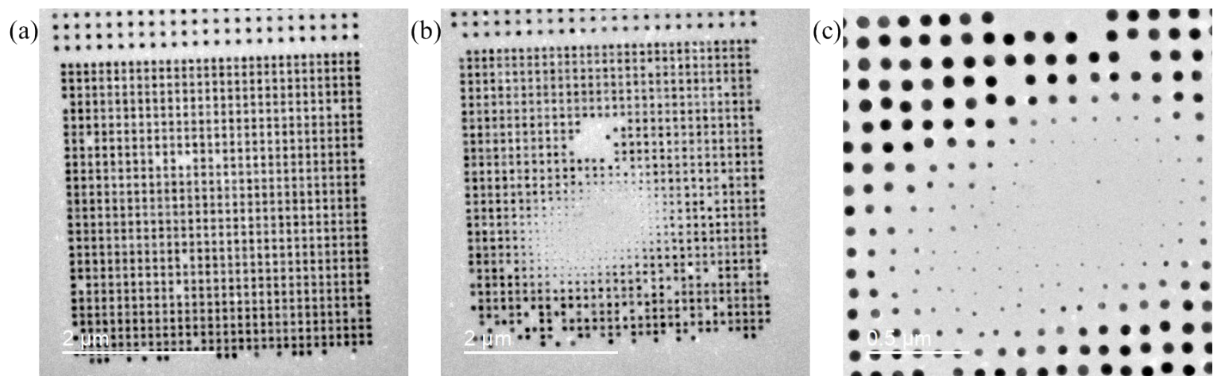


**Fig. S10** Bright field TEM images of (a) a pristine nanodisc array pattern on a silicon oxide membrane, (b) after a 30 mW green laser (532 nm) exposure for 4 minutes and (c) magnified area of the laser focused region showing nanodiscs degradation due to local heating. Scale bars are 2  $\mu\text{m}$ , 2  $\mu\text{m}$  and 0.5  $\mu\text{m}$  respectively. Gold nanodiscs are shown as dark contrast in the images due to electron scattering and absorption.

## 6. Bowtie Arrays Interspacing and LSPR

**Fig. S11** shows EEL spectra of two bowtie arrays with the same triangle height of 100 nm but separated by 20 nm and 100 nm from point to point. The upper spectra are extracted from the vertices and the lower spectra are extracted from the center of the triangle sides, as indicated by the blue boxed regions in the inset. The dipolar LSPR peak close to 1.8 eV is observed to slightly blue shift as the interspacing decreases, while the quadrupolar mode (at 2.3 eV) remains the same since it is not associated with other close triangles.

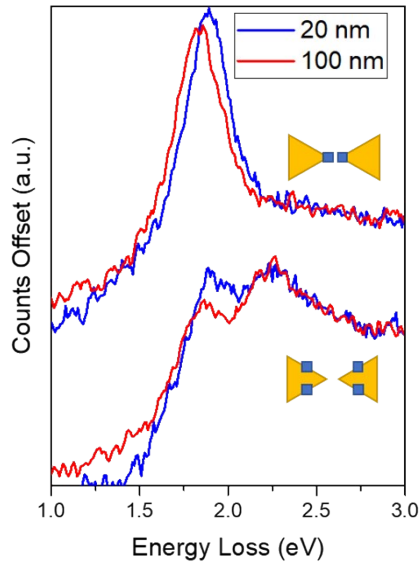


**Fig. S11** EEL spectra of two bowtie arrays with same size separated by 20 nm and 100 nm with the positions indicated by blue boxes in the insets. The dipolar mode ( $<2$  eV) slightly blue shifts as the interspacing is decreased, while the quadrupolar mode at 2.3 eV remains the same.

## 7. EELS Simulation of Bowtie Arrays

**Fig. S12** shows simulated EEL spectra from bowtie models composed of two 100 nm long triangular prisms, separated by a 50 nm gap, for the inner and outer vertices, midpoints of inner and outer edges. The hybridized anti-bonding dipolar mode is generated when the electron beam is placed within the gap region, while both the hybridized bonding and anti-bonding dipolar modes are generated when the beam is placed at the outer edge. The energy of bonding configuration is approximately 0.1 eV lower than that of the anti-bonding configuration in the electron energy loss spectrum. However, both modes of this bowtie could not be resolved in our experiment because of the  $\sim 160$  meV energy resolution, as demonstrated by the red curves which incorporated a 160 meV Lorentzian energy broadening. An additional quadrupolar mode is also excited when the beam is close to the inner bowtie edges.

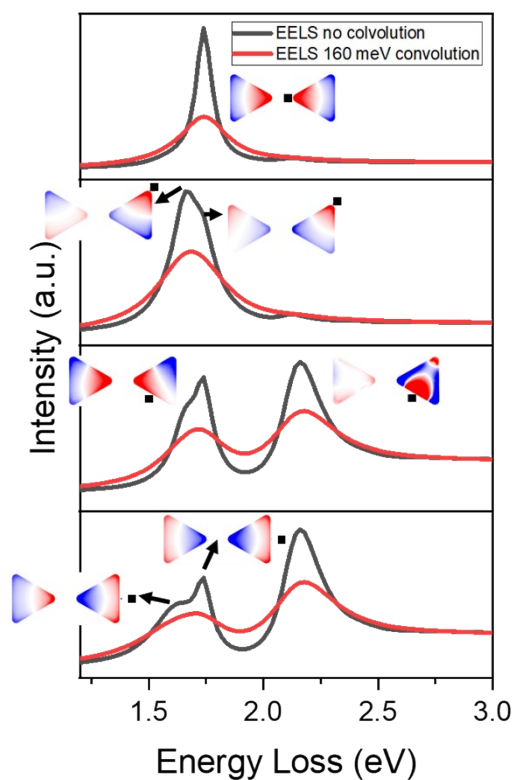


**Fig. S12** Simulated EEL spectra of 100 nm bowties in the inner vertex, outer vertex, the middle of inner edge and outer edge from top to bottom. Red curves are calculated from the black curves by convolving with a Lorentzian function at a full width half maximum of 160 meV. Insets are electron density distribution maps in the corresponding excitation locations marked by the black boxes showing dipole and quadrupole configurations. The bonding dipolar mode is extracted at an energy loss of 1.66 eV, the antibonding dipolar mode is extracted at 1.74 eV, and the quadrupolar mode is extracted at 2.16 eV. The corresponding electron density distributions of the bonding and antibonding dipolar modes are also pointed by arrows.

## 9. Bonding and Antibonding Dipolar Modes in 140 nm Sized Bowties

Larger bowties are less affected by the ZLP broadening due to better signal to noise ratio and exhibit the bonding and antibonding dipolar peak positions in the EEL spectra after background subtraction. Two Voigt profiles were used to fit the hybridized dipolar surface plasmon peak to separate the bonding and antibonding dipolar peaks of the 140 nm sized bowties as shown in **Fig. S13**. The fitted antibonding dipolar peak has stronger intensity and narrower FWHM, resulting in a higher quality factor. The fitted results were then used to estimate the SERS enhancement G from the bonding and antibonding dipolar modes as described in Methods.

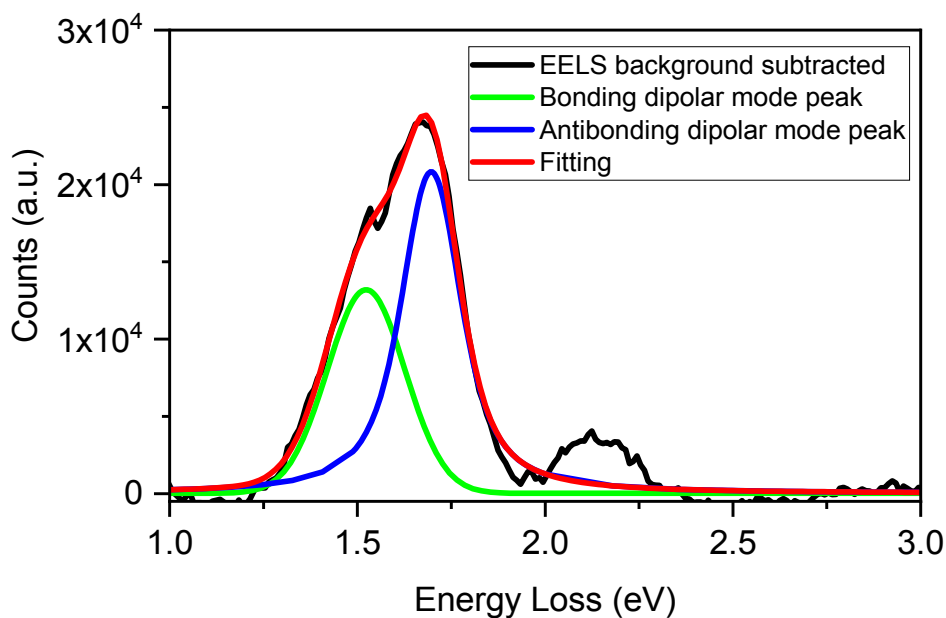


**Fig. S13** The bonding and antibonding dipolar surface plasmon peak fitting for 140 nm sized bowties separated by 20 nm gaps. Two Voigt profiles were used to fit the hybridized dipolar surface plasmon peaks using OriginPro software. The bonding dipolar peak is located at 1.52 eV with a full width at half maximum (FWHM) of 0.24 eV and the antibonding dipolar peak is located at 1.68 eV with a FWHM of 0.19 eV. The peak at 2.2 eV arises from partial excitation of quadrupolar modes.

## 10. Quadrupolar LSPR modes and Raman Spectra of Bowtie Arrays

**Fig. S14** shows Raman spectra of different size bowties on SiN<sub>x</sub> substrates collected using a 532 nm laser. The corresponding Raman signal collection region is indicated as the green shaded band in **main text Fig. 6a**, where the lower edge of the band is closer to the quadrupolar peak of 140 nm bowties. However, the enhancement from 1400 cm<sup>-1</sup> to 1700 cm<sup>-1</sup> (**Fig. S14** shaded region) is weaker than that of the smaller arrays. On the other hand, smaller arrays, with quadrupolar peak energy away from the lower energy edge of the band, show higher signal enhancement because the dipolar mode is closer to the lower edge of the band. Although there is no clear way to separately study the effect of dipolar and quadrupolar modes on Raman enhancement, **Fig. S14** provides indirect evidence that the quadrupolar mode is not effective in Raman signal enhancement.

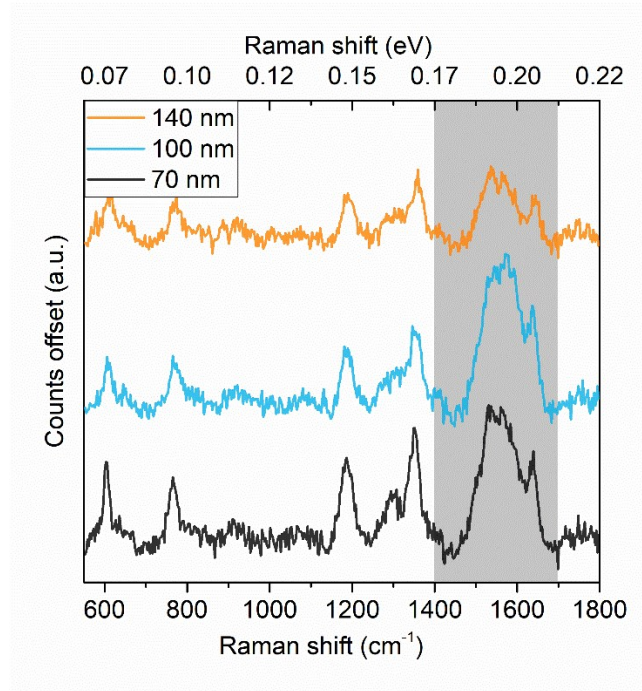


**Fig. S14** Raman spectra of different size bowties collected using a 532 nm laser. The Raman signal is not clearly enhanced when the laser energy is close to the quadrupolar peak, as evidenced by the relatively weaker Raman enhancement for 140 nm size bowties in the shaded area compared to that of the smaller bowties.

## Supplementary References

- (1) Maier, S. A. Localized Surface Plasmons. In *Plasmonics: Fundamentals and Applications*; Springer US: New York, NY, 2007; pp 65–88. [https://doi.org/10.1007/0-387-37825-1\\_5](https://doi.org/10.1007/0-387-37825-1_5).
- (2) GOULD, R. J. Classical Electrodynamics. In *Electromagnetic Processes*; John Wiley & Sons, Inc.: New York, 2020; pp 37–74. <https://doi.org/10.2307/j.ctv131bv37.5>.
- (3) Fröhlich, H. *Theory of Dielectrics*; Clarendon Press: Oxford, 1949.